

Received January 19, 2021, accepted January 31, 2021, date of publication February 10, 2021, date of current version June 24, 2021.

Digital Object Identifier 10.1109/ACCESS.2021.3058331

Electromagnetic Design of High-Speed and High-Thrust Cross-Shaped Linear Induction Motor

WEICHANG ZHOU^{ID}, ZHAOLONG SUN^{ID}, FENGRUI CUI^{ID}, AND YINHAO MAO^{ID}

School of Electrical Engineering, Naval University of Engineering, Wuhan 430033, China

Corresponding author: Fengrui Cui (fengruicui@foxmail.com)

ABSTRACT In order to improve the thrust density and efficiency of linear induction motors (LIM) in large load transport situations, a cross-shaped linear induction motors (CSLIM) structure is proposed in this paper. Firstly, for analyzing the characteristics of CSLIM, the magnetic field and electromagnetic thrust expression of long primary double-sided linear induction motors (LP-DSLIM) when considering the saturation of iron core are deduced, based on which the effect of iron saturation on electromagnetic thrust is analyzed. Secondly, the equivalent circuit of CSLIM is proposed and the effect of coupling on the electromagnetic thrust is analyzed. The results show that, the maximum electromagnetic thrust is reduced and the corresponding slip frequency is increased when iron saturation and coupling. For improving the problem of iron core saturation and coupling of CSLIM, a structure with square-type iron and lap winding is further proposed, and the rationality of CSLIM structure is verified by comparing the finite element simulation results of flux density on core, eddy current on secondary and the electromagnetic thrust.

INDEX TERMS CSLIM, electromagnetic thrust, equivalent circuit, iron saturation, coupling.

I. INTRODUCTION

Depending on the relative length of the primary and secondary of the linear induction motor (LIM), LIMs are divided into two types: long primary LIMs and short primary LIMs. The long primary double-sided linear induction motor (LP-DSLIM) shown in Fig. 1 is widely used in large load transport situations such as automotive accelerated collision tests [1]. In these situations with limited size, in order to improve the power density and thrust density, the motor works in high current conditions whose field inductance is reduced when the iron core is saturated, and the motor parameters may change due to the flux saturation that may result in degradation of the drive performance [2]. Therefore, the thrust and the efficiency are reduced that leads to few studies on the effects of iron saturation on LIM at home and abroad. Modeling of the LIMs was analyzed and law of the iron saturation was obtained from test data in paper [3]. It indicated that the iron was easily become saturated when current increased and slip frequency decreased. The paper [4] presented a research on magnetic circuit calculation and saturation characteristics analysis of the six-phase cylindrical linear induction motor. By this LIM distributed magnetic circuit method, the saturation coefficient and the magnetic

The associate editor coordinating the review of this manuscript and approving it for publication was Atif Iqbal^{ID}.

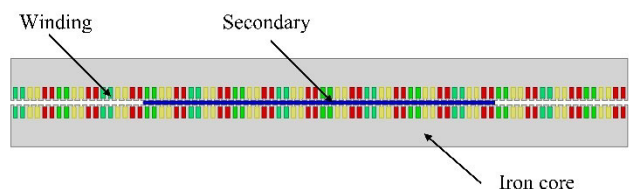


FIGURE 1. Two-dimensional model of LP-DSLIM.

density of each part of the motor can be calculated, and it almost has the same accuracy with finite element method. The nonlinear design method of LIM for urban rail transit system was proposed in paper [5] which considering the influence of saturation on the end effect. A novel slot-less LP-DSLIM was proposed in paper [6] for the application of electromagnetic launch. In this motor, the conventional gullet structure was cancelled, and conductive area of the motor stator windings was enlarged, and then the loss and temperature rise were decreased. The effect on magnetic field emission of saturated ferromagnetic core was analyzed in paper [7], and a simulation model for magnetic field emission analysis was established based on finite element method (FEM). The permeability of the saturated ferromagnetic core was solved through iterative computation, and then the magnetic field emission radiated by LIM was analyzed.

In order to improve the thrust density and efficiency of LIM, as well as improve reliability and redundancy,

paper [8]–[13] have studied a four-stator double-sided linear induction motor (FS-DSLIM). Paper [8] introduced a technique for FS-DSLIM based on the analysis of the relationship between coupling primaries. Calculation results in performances of terminal voltage and electromagnetic thrust were presented and compared with the test data. The coupling equivalent circuit model was built for FS-DSLIM in paper [9]. And based on the advanced coupling equivalent circuit model, the coupling characteristics of relevant physical quantities of the upper and lower stator and upper and lower equivalent windings of shuttle were analyzed. Furthermore, the relationships between the coupling characteristics and motor operation conditions were analyzed, and the operation conditions for mathematical decoupling of relevant physical quantities of shuttle upper and lower equivalent windings were studied. An analytical method to calculate the magnetic saturation factor of FS-DSLIM was proposed in paper [10]. In this method, the BH curve was simplified with a multi-line curve. An air-gap saturated factor expression, which was convenient for calculating the saturation inductance, was derived to describe the saturation effect of the iron. The edge gas magnetic coupling between up and down primaries in FS-DSLIM was analyzed in paper [11], and the current wave path coupling on the secondary was studied, based on which, for the different working conditions, the uniform lumped-parameter model was established, and the coupling parameters model were identified. In paper [12] the coupling effect of FS-DSLIM is studied with the 3-D finite-element method. The thrust force of the DSLIM with in-phase current is compared with the forces with inversed current and single stator excited. The relationship between electromagnetic thrust, phase current and slip frequency of FS-DSLIM is particularly analyzed in paper [13]. Then the phase current overload rule is obtained when one primary fails and the other primary works to keep the electromagnetic thrust unaltered.

Electromagnetic thrust is the most critical performance of LIM. The thrust fluctuations caused by the impedance imbalance are analyzed in paper [14], [15]. Composition and characteristics of electromagnetic thrust were obtained in paper [14], and paper [15] suggested a harmonic injection method to reduce the thrust fluctuation. Time-harmonic analytical solution of thrust based on the secondary coordinate system was derived in paper [16], as well as the characteristics of all thrust components vs. slip frequency. In order to improve the electromagnetic thrust, various type of secondary was used in paper [17]–[19], such as ladder-slit secondary in paper [17], v-type secondary in paper [18] and cap-lamination secondary in paper [19].

Above all, for improving the thrust density and efficiency of high-speed and high-thrust LIM, it can be achieved by improving problems of iron saturation, coupling and end effect, including the use of slot-less iron, multiple primaries sharing the same secondary, improving the primary winding and secondary structure. This paper proposes a structure of cross-shaped linear induction motor (CSLIM), deduces the expressions of air-gap magnetic density and electromagnetic

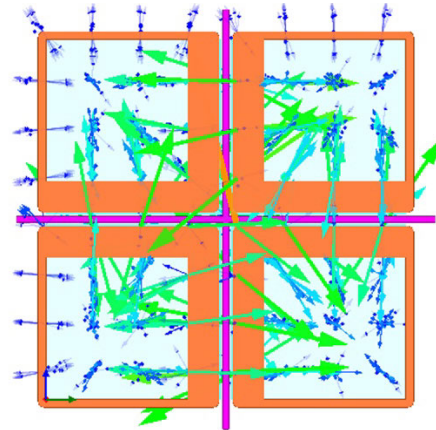


FIGURE 2. The magnetic density distribution of CSLIM.

thrust of LP-DSLIM which considering iron saturation, analyzes the effect of iron saturation on electromagnetic thrust, and verifies it by FEM. In order to analyze the characteristics of CSLIM, the equivalent circuit is given, and the electromagnetic thrust expression is inferred based on it. The effect of electromagnetic coupling on thrust is analyzed which is verified by FEM. For improving problems of iron saturation and electromagnetic coupling, a CSLIM structure with square-type iron and lap winding is proposed, and the rationality of CSLIM structure is verified by comparing the simulation results of magnetic density, inductive eddy current on secondary and electromagnetic thrust.

II. STRUCTURE OF CSLIM

LP-DSLIM is used in large load transport situations such as electromagnetic launch. The LP-DSLIM consists of a symmetrical primary, which is wrapped around three-phase windings, and a secondary consisting of aluminum plate. The three-phase winding is electrified to generate a magnetic field wave, which will sense the inductive eddy current on secondary, thus generating electromagnetic thrust in the direction of the magnetic field wave.

Since both the primary and secondary ends of the LIM are open and the air gap of LIM for large load transport is generally large, its efficiency is often lower than that of RIM. Paper [8]–[13] have proposed a four-stator double-sided induction motor structure (FS-DSLIM). FS-DSLIM acts on the same aluminum plate, which effectively improves thrust density and efficiency. However, the research shows that there is magnetic coupling between the two primary pairs as shown in Fig. 2, and the inductive eddy current coupling on the secondary is shown in Fig. 3, the presence of coupling increases the loss, which is not conducive to the improvement of electromagnetic thrust and efficiency.

In order to further improve the thrust density and efficiency, a cross-shaped structure of LIM (CSLIM) is proposed, as shown in Fig. 4. It consists of a cross-shaped secondary with four primary iron distributed at four angles symmetrically, each with a three-phase ringing winding in the groove.

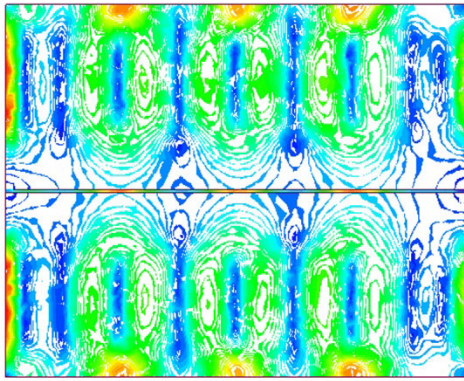


FIGURE 3. The inductive eddy current distribution of CSLIM.

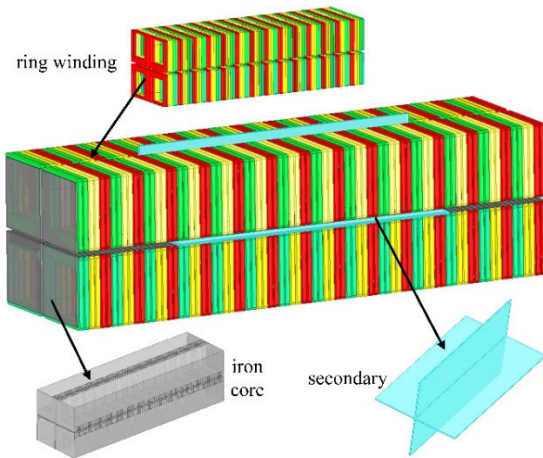


FIGURE 4. The structure schematic of CSLIM.

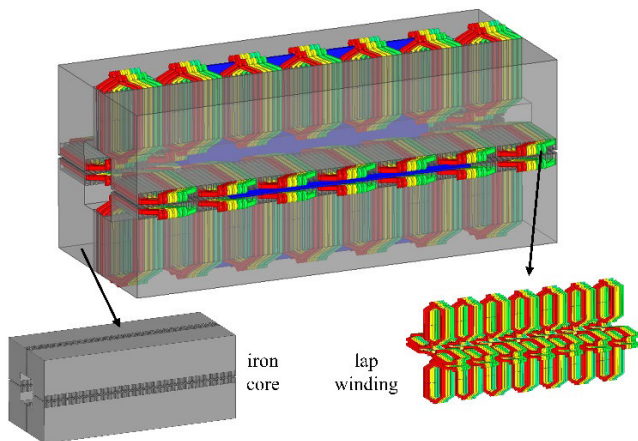


FIGURE 5. The improved structure schematic of CSLIM.

For improving the problem of iron saturation and coupling, a CSLIM structure with a square-type iron and lap winding is proposed, as shown in Fig. 5.

III. THRUST ANALYSIS OF DSLIM

A. THEORETICAL MODEL

In electromagnetic field analysis, the higher the dimensionality of the field, the more accurate the calculation results,

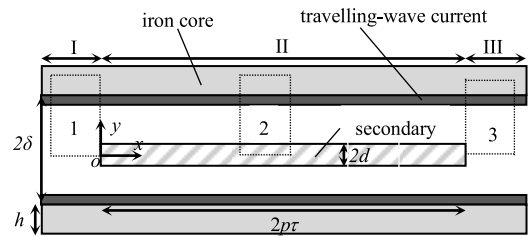


FIGURE 6. Two-dimension electromagnetic field model of LP-DSLIM.

but the more complex the solution process. The distribution of LIM magnetic field and current belongs to the three-dimensional field, but after some simplified hypothesis, one-dimensional field analysis can be used. The theoretical analysis model is shown in Fig. 6.

LP-DSLIM consists of primary which is upper and lower distributed, where has a winding with three-phase currents, the primary core thickness is h . The secondary length is $2p\tau$, the secondary thickness is $2d$, and the equivalent air-gap length is 2δ . The x direction is the secondary motion direction and the y direction is the air gap direction. The basic assumptions are as follows: 1) \mathbf{H} and \mathbf{B} have only y component, all currents only have z component; 2) all field quantities are only functions about x in space; 3) the magnetic potential generated by primary winding currents is spatial sine distributed, i.e. only considering the fundamental wave; 4) replace the primary winding with an equivalent layer of travelling-wave current.

B. AIR-GAP MAGNETIC FIELD EXPRESSION

The basic equations for theoretical analysis of LIM are

$$\begin{cases} \nabla \times \mathbf{H} = \mathbf{j}_1 + \mathbf{j}_2 \\ \nabla \times \mathbf{E} = -\frac{\partial \mathbf{B}}{\partial t} \\ \nabla \cdot \mathbf{B} = 0 \\ \mathbf{j}_2 = \sigma (\mathbf{E} + \mathbf{v} \times \mathbf{B}) \end{cases} \quad (1)$$

where, \mathbf{H} is magnetic field intensity, \mathbf{B} is magnetic flux density, \mathbf{E} is electric field intensity, \mathbf{j}_1 and \mathbf{j}_2 are primary and secondary current density respectively. \mathbf{v} is secondary speed, σ is the conductivity of secondary.

According to ampere circuital theorem, take the integral path of the dotted rectangle 2 in Fig. 6

$$\frac{\partial B_\delta}{\partial x} \cdot \frac{\delta}{\mu_0} + \int \frac{1}{\mu_0 \mu_r K_{fe} h} \cdot \frac{\partial B_\delta}{\partial x} dx = \mathbf{j}_1 + \mathbf{j}_2 d \quad (2)$$

where, μ_0 is the permeability of vacuum, μ_r is the relative permeability of the primary iron, and K_{fe} is the stacking factor of the iron.

By faraday law of electromagnetic induction

$$\frac{\partial E_\delta}{\partial x} = \frac{\partial B_\delta}{\partial t} \quad (3)$$

According to assumption 3), the equivalent layer of travelling-wave current can be set to

$$\mathbf{j}_1 = J_1 e^{j(\omega t - \beta x)} \quad (4)$$

where, $J_1 = \sqrt{2}m_1N_1k_{w1}I/p\tau$ is value of the equivalent layer of travelling-wave current, $\beta = \pi/\tau$, m_1 is the number of phases, N_1 is the number of turns per phase winding, k_{w1} is the winding coefficient, I is effective value of the primary phase current, p is the pole pairs corresponding to the length of secondary, τ is the polar pitch.

According to (4), we can take the derivative of x , it's available that

$$\frac{\partial j_1}{\partial x} = -j\beta j_1 \quad (5)$$

According to (1), we can take the derivative of x , and substitute (3) for it, it's available that

$$\frac{\partial j_2}{\partial x} = \sigma \left(\frac{\partial B_\delta}{\partial t} + v \frac{\partial B_\delta}{\partial x} \right) \quad (6)$$

According to (2), we can take the derivative of x , and substitute (5) and (6) for it, it's available that

$$\frac{\partial^2 B_\delta}{\partial x^2} - (\sigma_e v \mu_0 - C_1) \frac{\partial B_\delta}{\partial x} - \sigma_e \mu_0 \frac{\partial B_\delta}{\partial t} = -j \frac{\beta \mu_0}{\delta} j_1 \quad (7)$$

where, $\sigma_e = \sigma d/\delta$, $C_1 = 1/\delta \mu_r K_{fe} h$.

When solving the particular solution of (7), we can order

$$B_{\delta 0} = B_m e^{j(\omega t - \beta x + \alpha)} \quad (8)$$

Substituting (8) into (7) gives

$$\begin{cases} B_m = \frac{\mu_0 J_1}{\delta \beta \sqrt{1 + (sG + C_1/\beta)^2}} \\ \alpha = \tan^{-1} \left(\frac{-1}{sG + C_1/\beta} \right) \end{cases} \quad (9)$$

When solving the general solution of (7), we can order

$$B_\delta = T(t) X(x) \quad (10)$$

Substituting (10) into (7) gives

$$B_{\delta 1,2} = A_1 e^{-\frac{x}{\lambda_1}} e^{j(\omega t - \frac{\pi}{\tau_e} x)} + A_2 e^{\frac{x}{\lambda_2}} e^{j(\omega t + \frac{\pi}{\tau_e} x)} \quad (11)$$

$\lambda_1 = 2/k_1(-1 + \sqrt{(1+k_2)/2})$ is attenuation constant of the enter-travelling wave, $\lambda_2 = 2/k_1(1 + \sqrt{(1+k_2)/2})$ is attenuation constant of the exit-travelling wave, $\tau_e = 2\pi/k_1\sqrt{(-1+k_2)/2}$ is the half-wavelength of them. They are all produced by the dynamic end effect.

Thus, the air-gap magnetic field expression in area II shown in Fig. 6 is given

$$B_\delta = B_{\delta 0} + B_{\delta 1,2} \quad (12)$$

Since areas I and III do not contain secondary, the integration paths of dotted rectangles 1 and 3 in Fig. 6 are available

$$\frac{\partial B_\delta}{\partial x} \cdot \frac{\delta}{\mu_0} + \int \frac{1}{\mu_0 \mu_r K_{fe} h} \cdot \frac{\partial B_\delta}{\partial x} dx = j_1 \quad (13)$$

Similarly, the air-gap magnetic field expressions in areas I and III can be given respectively

$$\begin{cases} B_{\delta I} = B_{m1} e^{j(\omega t - \beta x + \alpha_1)} \\ B_{\delta III} = B_{m1} e^{j(\omega t - \beta(x-2p\tau) + \alpha_1)} \end{cases} \quad (14)$$

where, $B_{m1} = \frac{\mu_0 J_1}{\delta \beta \sqrt{1 + (C_1/\beta)^2}}$, $\alpha_1 = \tan^{-1} \frac{-\beta}{C_1}$.

Depending on the boundary conditions

$$\begin{cases} H_\delta |_{x=0} = H_{\delta I} |_{x=0} \\ H_\delta |_{x=2p\tau} = H_{\delta III} |_{x=2p\tau} \end{cases} \quad (15)$$

Using (11) and (14), it's available that (16) and (17), as shown at the bottom of the page.

Substituting (16) or (17) into (11), it's available to get magnetic field expressions in area II.

C. ELECTROMAGNETIC THRUST CALCULATION

The average thrust of DSLIM acting on the secondary can be calculated in the lower formula

$$F = 2 \times 2a \int_0^{2p\tau} 0.5 \operatorname{Re} (j_1^* \cdot B_\delta) dx \quad (18)$$

If only the electromagnetic thrust generated by the fundamental wave of magnetic field is taken into account, substituting (4) and (8) into (18) gives

$$F = \frac{4ap\tau \mu_0 J_1^2 (sG + C_1/\beta)}{\delta \beta [1 + (sG + C_1/\beta)^2]} \quad (19)$$

In order to verify the correctness of the above theoretical analysis, the motor parameters are designed with a maximum thrust of 4KN and a synchronous speed of 68m/s as shown in Table 1. The LP-DSLIM is simulated with JMAG.

For facilitating simulation and experimental, the locked-rotor test is used to verify. At this time, the average thrust

$$\begin{cases} A_1 = \frac{B_{m1} e^{j\alpha_1} (e^{Q_2} - 1) - B_m e^{j\alpha} (e^{Q_2} + 1)}{e^{Q_2} - e^{-Q_1}} \quad _2p = 1, 3, 5 \dots \\ A_1 = \frac{(B_{m1} e^{j\alpha_1} - B_m e^{j\alpha}) (e^{Q_2} - 1)}{e^{Q_2} - e^{-Q_1}} \quad _2p = 2, 4, 6 \dots \end{cases} \quad (16)$$

$$\begin{cases} A_2 = \frac{B_{m1} e^{j\alpha_1} (e^{-Q_1} - 1) - B_m e^{j\alpha} (e^{-Q_1} + 1)}{e^{-Q_1} - e^{Q_2}} \quad _2p = 1, 3, 5 \dots \\ A_2 = \frac{(B_{m1} e^{j\alpha_1} - B_m e^{j\alpha}) (e^{-Q_1} - 1)}{e^{-Q_1} - e^{Q_2}} \quad _2p = 2, 4, 6 \dots \end{cases} \quad (17)$$

TABLE 1. Electromagnetic parameters of prototype.

| Item | Value |
|---|-------------------|
| Pole pitch τ (m) | 0.084 |
| Thickness of secondary $2d$ (mm) | 5 |
| Electrical conductivity of secondary σ_c (S/m) | 5.6×10^7 |
| Equivalent air-gap length 2δ (mm) | 9 |
| Number of turns per slot N | 4 |
| Slot depth (mm) | 28 |
| Yoke thickness (mm) | 50 |
| Slot width (mm) | 10 |
| Length of secondary (m) | 0.672 |
| Tooth width (mm) | 4 |
| Number of slots per pole and phase | 2 |
| Width of primary (mm) | 160 |
| Width of secondary (mm) | 214 |

caused by the fundamental wave is consistent with that when the secondary is in motion, but the average thrust caused by the enter-travelling wave and exit-travelling wave have a large difference between these two cases, so the influence of end effect on the air-gap magnetic field cannot be ignored. At the same time, in order to avoid the effects of saturation, the effective value of primary current is set to 0.3A. Fig. 7 shows the difference between the theoretical value and the simulation value of the LP-DSLIM's electromagnetic thrust vs. slip frequency. As can be seen from the figure, the theoretical and simulation results are basically consistent.

IV. ANALYSIS OF ELECTROMAGNETIC THRUST

A. THE EFFECT OF IRON SATURATION ON ELECTROMAGNETIC THRUST

According to (19), we can take the derivative of s , and order $\partial F / \partial s = 0$, it's available that

$$F_{\max} = \frac{2ap\tau\mu_0J_1^2}{\delta\beta} \tag{20}$$

The slip frequency at this time is

$$f_{\max} = sf = \left(1 - \frac{C_1}{\beta}\right) \frac{f}{G} = \left(1 - \frac{C_1}{\beta}\right) \frac{\pi\delta}{2\mu_0\sigma_s\tau^2} \tag{21}$$

It can be seen from (21) that the saturation of the iron core increases C_1 , while the increase of C_1 has no effect on the maximum thrust caused by the fundamental wave, but reduces the slip frequency corresponding to the maximum thrust. However, in fact, iron saturation will also lead to an increase in the thickness of the equivalent air gap, which in turn will result in a decrease in the maximum thrust, and the corresponding slip frequency is increased.

Fig. 8 shows the relationship of the electromagnetic thrust with slip frequency when current is 300A or 0.3A. As can be seen from Fig. 8, when current is 300A, the maximum value of the thrust is about 3774N when the iron is saturated,

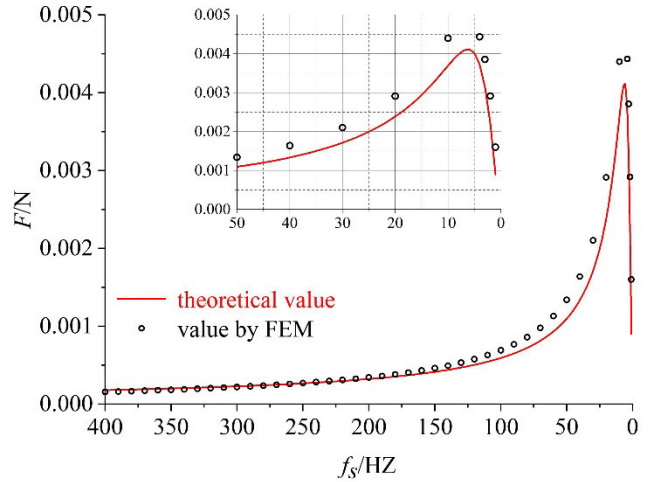


FIGURE 7. Curve of thrust vs. slip frequency of DSLIM when $I=0.3A$.

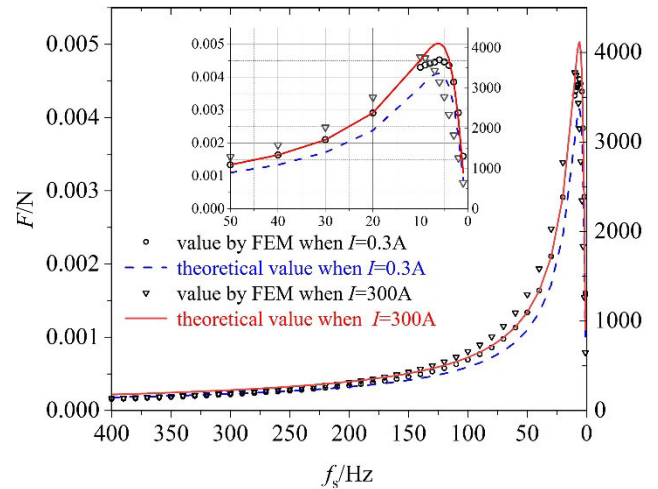


FIGURE 8. Curve of thrust vs. frequency of DSLIM when $I=300A$ or $0.3A$.

while it is about 4116N when regardless of saturation, which is reduced about 8.3%, and the corresponding slip frequency is increased from 6Hz to 10Hz.

The magnetic density graph of CSLIM at 300A current is shown in Fig. 9. As can be known from Fig. 9, due to the use of ring windings, the saturation of the iron is serious, which is not conducive to improving the thrust density and efficiency.

B. EQUIVALENT CIRCUIT

In order to facilitate the analysis of the operating characteristics of motor, the equivalent circuit is generally used [20]. In [21], a T-model equivalent circuit is proposed which considering the transversal edge and longitudinal end effects and the half-filled slots at the primary ends. The longitudinal end effects are estimated using three different impedances representing the normal, forward, and backward flux density waves in the air gap in [22]. Based on equivalent circuit, [23] makes a comprehensive efficiency optimization to LIM efficiency from both motor design and control aspects.

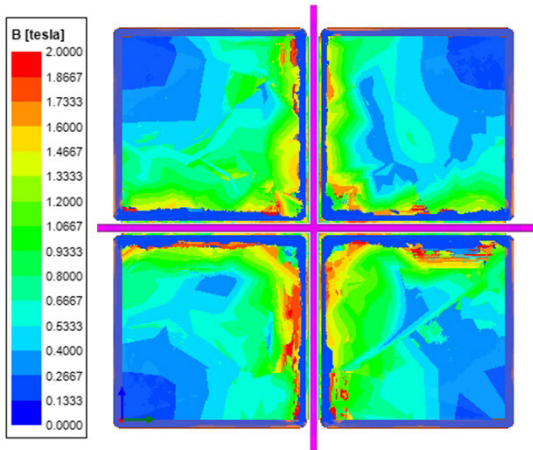


FIGURE 9. Magnetic density graph of CSLIM on stator core.

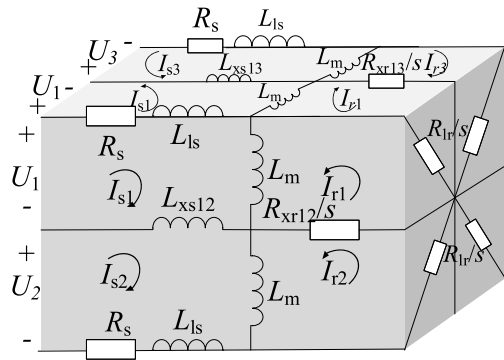


FIGURE 10. The equivalent circuit of CSLIM.

The CSLIM equivalent circuit given in this paper is shown in Fig. 10, where the parameter meaning is shown in Table 2. Focusing on the analysis of the two typical working conditions, i.e. equal current size and equal phase ($I_{r1} = I_{r4}, I_{r2} = I_{r3}$) and equal current size but opposite phase ($I_{r1} = -I_{r4}, I_{r2} = -I_{r3}$).

When $I_{r1} = I_{r4}, I_{r2} = I_{r3}$, taking Primary 1 as an example, according to the equivalent circuit, the voltage equation of secondary-side can be obtained

$$\begin{cases} j\omega_s L_m (I_{s1} + I_{r1}) + I_{r1} (R_{lr} + R_{xr12}) - I_{r2} R_{xr12} = 0 \\ j\omega_s L_m (I_{s1} + I_{r1}) + I_{r1} (R_{lr} + R_{xr13}) - I_{r3} R_{xr13} = 0 \\ j\omega_s L_m (I_{s1} + I_{r1}) + I_{r1} (R_{lr} + R_{xr14}) - I_{r4} R_{xr14} = 0 \end{cases} \quad (22)$$

According to (22), it's available that

$$|I_{r1}| = |I_{r2}| = |I_{r3}| = |I_{r4}| = \left| I_{s1} \frac{-j\omega_s L_m}{j\omega_s L_m + R_{lr}} \right| \quad (23)$$

At this point, the electromagnetic thrust of CSLIM is

$$F_e = \frac{3 \times 4 \times (I_{r1})^2 R_{lr}}{v_s} = \frac{12 I_{s1}^2 L_m^2 \beta \omega_s R_{lr}}{R_{lr}^2 + \omega_s^2 L_m^2} \quad (24)$$

TABLE 2. Equivalent parameters of CSLIM.

| Symbol | Meaning |
|----------|----------------------------|
| L_m | Exciting inductance |
| L_{ls} | Leakage inductance |
| L_{xs} | Coupling inductance |
| R_{lr} | Secondary resistance |
| R_{xr} | Coupling resistance |
| I_s | Phase current of primary |
| I_r | Phase current of secondary |
| R_s | Primary resistance |
| U | Phase voltage |

We can take the derivative of (24), the maximum electromagnetic thrust of the constant current is

$$F_{e \max} = 6 I_{s1}^2 \beta L_m \quad (25)$$

The corresponding slip frequency is

$$\omega_{s \max} = \frac{R_{lr}}{L_m} \quad (26)$$

Due to the increase in the thickness of the equivalent air gap when considering iron saturation, the magnetic inductance is reduced which will cause the maximum electromagnetic thrust to decrease, and the corresponding slip frequency increases, that is consistent with the conclusion obtained by (21).

The primary resistance R_s , primary leakage inductance L_{ls} , secondary resistance R_{lr} , and exciting inductance L_m can be calculated based on the structural dimensions of the machine [21]. Due to the nonlinear magnetization characteristic of the rotor core, saturation may appear at some operating conditions and should be considered. Permeability of the back iron μ at each slip frequency can be obtained by FEM [24].

C. THE EFFECT OF COUPLING ON THRUST

When $I_{r1} = -I_{r4}, I_{r2} = -I_{r3}$, it's available that

$$\begin{cases} |I_{r1}| = |I_{r4}| = \left| I_{s1} \frac{-j\omega_s L_m}{j\omega_s L_m + R_{lr} + 2R_{xr14}} \right| \\ |I_{r2}| = |I_{r3}| = \frac{R_{xr12} - 2R_{xr14}}{R_{xr12}} |I_{r1}| \end{cases} \quad (27)$$

At this point, the electromagnetic thrust of CSLIM is

$$F_e = \frac{12 I_{s1}^2 L_m^2 \beta \omega_s R_{lr} (R_{xr12}^2 - 2R_{xr12} R_{xr14} + 2R_{xr14}^2)}{[(R_{lr} + 2R_{xr14})^2 + \omega_s^2 L_m^2] R_{xr12}^2} \quad (28)$$

We can take the derivative of (28), the maximum electromagnetic thrust of the constant current is

$$F_{e \max} = \frac{6 I_{s1}^2 \beta L_m R_{lr} (R_{xr12}^2 - 2R_{xr12} R_{xr14} + 2R_{xr14}^2)}{(R_{lr} + 2R_{xr14}) R_{xr12}^2} \quad (29)$$

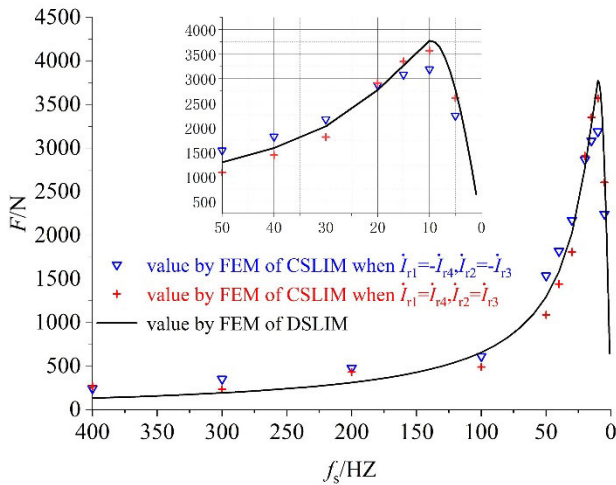


FIGURE 11. Curve of thrust vs. slip frequency of two working conditions.

The corresponding slip frequency is

$$\omega_{s \max} = \frac{R_{lr} + 2R_{xr14}}{L_m} \quad (30)$$

It can be known through comparing (25) and (26) with (29) and (30) that, the presence of coupling resistors R_{xr12} and R_{xr14} reduces the electromagnetic thrust, and the corresponding slip frequency is increased. Fig. 11 shows the electromagnetic thrust of the CSLIM that shown in Fig. 5 in the two working conditions, i.e. condition ① $I_{r1} = I_{r4}$, $I_{r2} = I_{r3}$ and condition ② $I_{r1} = -I_{r4}$, $I_{r2} = -I_{r3}$ when the current is 300A. As can be known by comparison, the electromagnetic thrust produced by a single primary unit is about 3572N, but due to the presence of coupling resistance, the electromagnetic thrust is only about 3191N, which is reduced about 10.7%. It is shown that coupling has a great influence on electromagnetic thrust, and the motor should use condition ①.

In the proposed equivalent circuit model, coupling resistance R_{xr} can be obtained by the FEM with different working conditions.

The magnetic coupling and inductive eddy current coupling at 300A current are shown in Fig. 2 and Fig.12, respectively, and it can be known from Fig. 2 that there is a significant magnetic coupling between the four ring windings of CSLIM, which is not conducive to improving the thrust density and efficiency. At the same time by Fig. 12, it can be known that there is inductive eddy current coupling between the secondary aluminum plate, which is also not conducive to improving the thrust density and efficiency.

V. STRUCTURAL IMPROVEMENT

From the above analysis, it can be known that there is obvious magnetic coupling in CSLIM, and the iron saturation is serious, and there is also inductive eddy current coupling in secondary aluminum plate. These phenomena reduce the electromagnetic thrust, which is not conducive to improving the thrust density and efficiency. In order to improve the

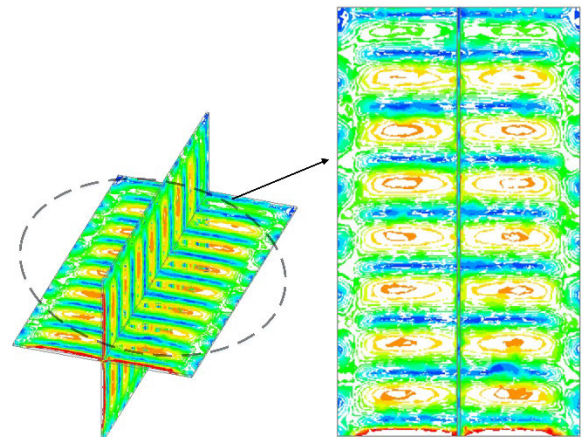


FIGURE 12. Induced eddy current graph of CSLIM.

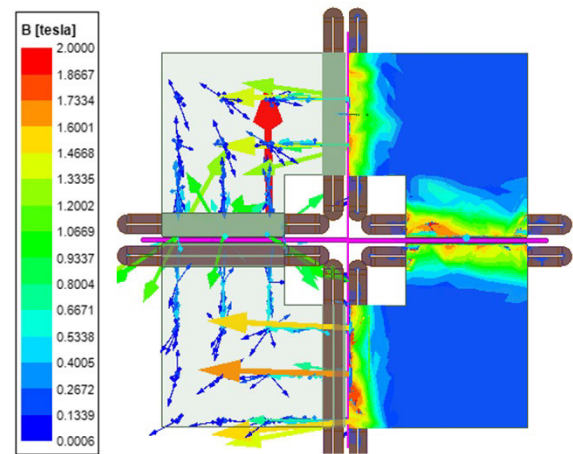


FIGURE 13. Magnetic density graph of improved CSLIM.

above problems, this paper optimizes the motor structure shown in Fig. 4, and proposes a CSLIM structure with a square-shaped iron and lap winding as shown in Fig. 5. In order to improve the problem of iron saturation, the lap winding is used. Meanwhile, the coupling problem can be improved by using the square-shaped iron which can increase the distance between the four windings appropriately.

As shown in Fig. 13, the left and right sides correspond to the same working conditions as shown in Fig. 2 and Fig. 9, it can be seen by comparison that, the iron saturation and magnetic field coupling problems are improved. Fig. 14 shows the induced eddy current graph of the corresponding working conditions in Fig. 12, it can be seen by comparison that, inductive eddy current coupling problem is improved.

Fig. 15 shows the curve of electromagnetic thrust vs. slip frequency of the two structures under the same working conditions, and by comparison, the thrust produced by a single primary unit of the improved structure is about 3572N, while it is about 3211N before the improvement, which is about 11.2% higher, indicating that its improvement on the problem of iron saturation and coupling is obvious.

Since this type of motor is used in electromagnetic launch applications, in order to achieve the end speed of the design

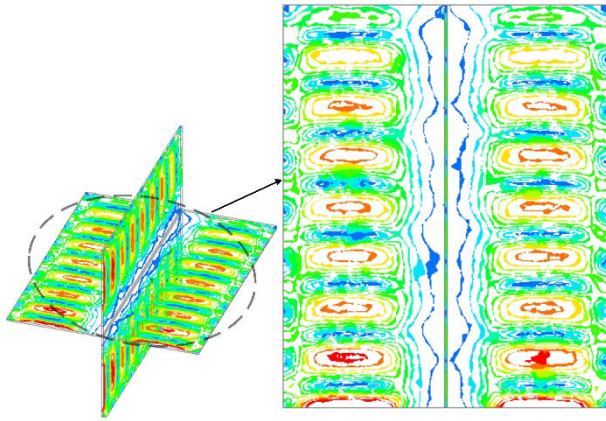


FIGURE 14. Induced eddy current graph of improved CSLIM.

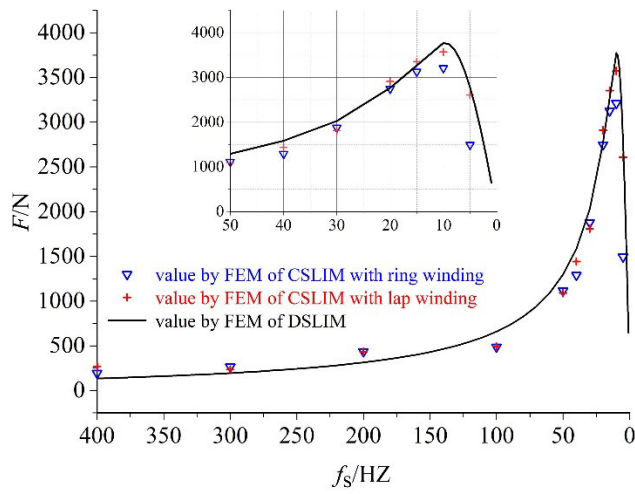


FIGURE 15. Thrust comparison of two type CSLIM.

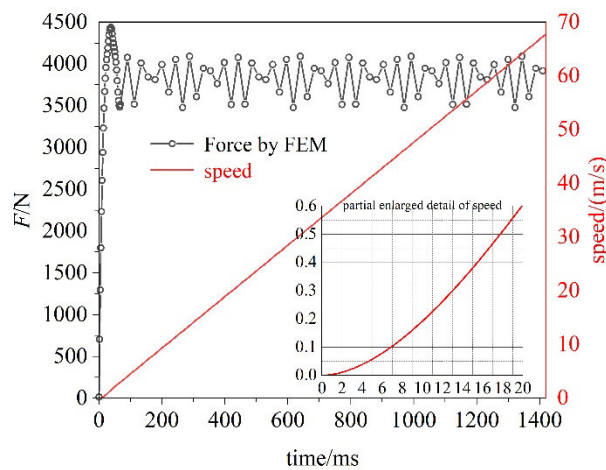


FIGURE 16. Thrust and speed of CSLIM vs time.

as soon as possible (the end speed of the sample is 67.7m/s), the motor uses constant slip frequency control. As can be known from Fig. 8, the motor has the largest thrust when the slip frequency is 10Hz. For ensuring the safety of personnel and equipment at launch, the acceleration of the launch must

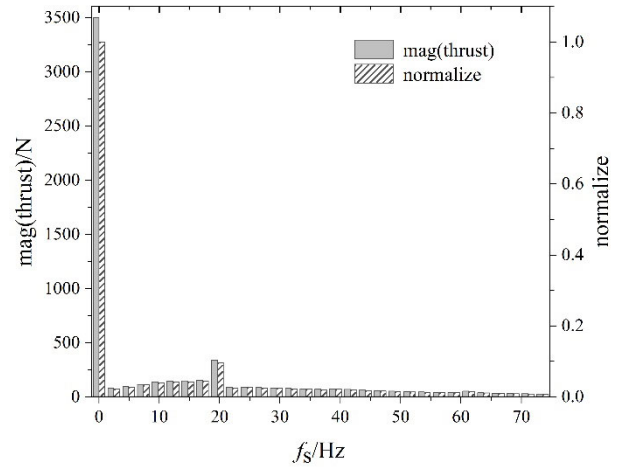


FIGURE 17. fast fourier transform of thrust.

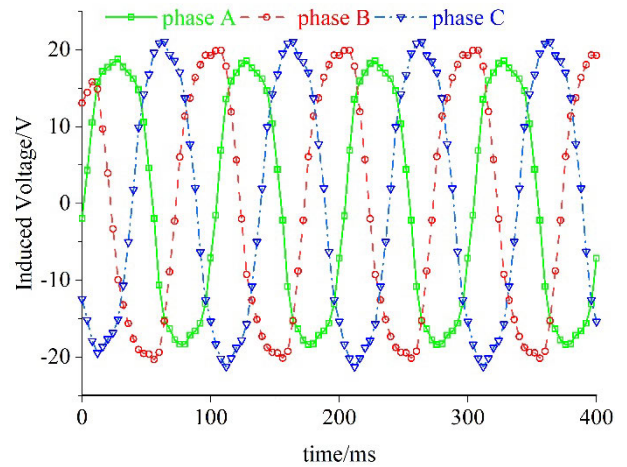


FIGURE 18. induced voltage vs time.

not be too large (designed not to exceed 50m/s²). When the load mass is 320kg, the acceleration process and the single primary thrust vs time are shown in Fig. 16. As can be shown from Fig. 16, the motor thrust fluctuates by about 8% and the acceleration process is smooth. The fast fourier transform of thrust is shown in Fig. 17, the average thrust portion (i.e. 0Hz) is about 3500N, and the thrust fluctuation portion (twice the slip frequency, i.e. 20Hz) caused by the forward-end effect is about 337N, about 9% of the average thrust. When the motor uses a current source, due to the asymmetry of the three-phase impedance, the three induced voltage are asymmetric, as shown in Fig. 18.

VI. CONCLUSION

For improving the thrust density and efficiency of LIM, CSLIM is proposed, the effects of iron saturation and coupling on the electromagnetic thrust of the motor is analyzed based on the equivalent circuit, which are verified by FEM. The results show that:

- 1) Iron saturation will reduce the maximum electromagnetic thrust of CSLIM, and the corresponding slip frequency increases;

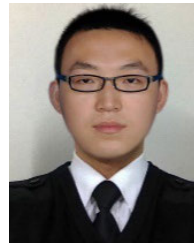
- 2) The magnetic coupling and induced eddy current electromagnetic coupling will reduce the maximum thrust of CSLIM, and the corresponding slip frequency increases;
- 3) Structural improvement can ameliorate iron saturation and electromagnetic coupling problems;
- 4) For improving the thrust density and efficiency of CSLIM, the working condition with the same size and phase of current should be adopted.

REFERENCES

- [1] S. E. Abdollahi, M. Mirzayee, and M. Mirsalim, "Design and analysis of a double-sided linear induction motor for transportation," *IEEE Trans. Magn.*, vol. 51, no. 7, pp. 1–7, Jul. 2015.
- [2] D. Perdukova, P. Palacky, P. Fedor, P. Bober, and V. Fedak, "Dynamic identification of rotor magnetic flux, torque and rotor resistance of induction motor," *IEEE Access*, vol. 8, pp. 142003–142015, 2020.
- [3] Z. Sun, D. Liu, W. Ma, J. Lu, Y. Zhang, J. Xu, and H. Yang, "Modeling and parameters of linear induction motors with iron saturation," in *Proc. CSEE*, 2011, vol. 31, no. 33, pp. 144–149.
- [4] H. Chuibing, M. Weiming, and X. Jin, "Magnetic circuit calculation and saturation characteristics analysis of six phase cylindrical linear induction motor," *Trans. China Electrotech. Soc.*, vol. 33, no. 5, pp. 1032–1039, 2018.
- [5] M. Yujie and C. Jianyun, "Nonlinear design of linear induction motors in urban rail transit," *Adv. Technol. Elect. Eng. Energy*, vol. 25, no. 3, pp. 59–62, 2006.
- [6] X. Jin, Y. Xidang, M. Weiming, Z. Yuxing, and S. Zhaolong, "Nonlinear calculation methods of long primary double-sided linear induction motor," in *Proc. 17th Int. Conf. Electr. Mach. Syst. (ICEMS)*, Oct. 2014, pp. 1774–1778.
- [7] X. Zhang, Z. Zhao, and P. Meng, "Simulation analysis for magnetic field emission of saturated linear motor," *Ship Sci. Technol.*, vol. 36, no. 6, pp. 102–105, 2014.
- [8] Z. Sun, W. Ma, D. Liu, J. Lu, J. Xu, and Y. Zhang, "Modeling and parameter measurement scheme for double primaries coupling linear induction motors," in *Proc. 19th Int. Conf. Electr. Mach. (ICEM)*, Sep. 2010, pp. 1–5.
- [9] X. Jin, M. Weiming, L. Junyong, S. Zhaolong, and Z. Yuexing, "The mathematical model and performance analysis of a novel four-stator double-sided linear induction motor," in *Proc. Int. Conf. Electr. Mach. Syst.*, 2011, pp. 1–6, doi: [10.1109/ICEMS.2011.6073932](https://doi.org/10.1109/ICEMS.2011.6073932).
- [10] Y. Zhang, M. Ma, W. Ma, J. Lu, J. Xu, and Z. Sun, "Analysis of saturation characteristics of double-stator linear induction motors," in *Proc. CSEE*, 2012, vol. 32, no. 36, pp. 102–107.
- [11] M. Ma, W. Ma, Y. Zhang, G. Wang, and W. Li, "Lumped parameter model of double-primary linear induction motor," *Electr. Mach. Control*, vol. 16, no. 1, pp. 1–5, 2012.
- [12] Y. Zhang, M. Zhang, W. Ma, J. Xu, J. Lu, and Z. Sun, "Modeling of a double-stator linear induction motor," *IEEE Trans. Energy Convers.*, vol. 27, no. 3, pp. 572–579, Sep. 2012.
- [13] M. Ma, W. Ma, Y. Zhang, D. Guo, G. Wang, and X. Cui, "Phase current overload characteristics of multi-primary linear induction motors under failure modes," in *Proc. CSEE*, 2013, vol. 33, no. 18, pp. 96–101.
- [14] Z. Han, J. Xu, W. Rui, and Y. Wang, "Effect of winding connections on thrust and current asymmetry of linear induction machines considering end effect," *IEEE Trans. Plasma Sci.*, vol. 48, no. 8, pp. 2816–2821, Aug. 2020.
- [15] N. Shixiong, S. Zhaolong, M. Weiming, M. Mingzhong, X. Jin, and L. Junyong, "Thrust ripple research on linear induction motors," *Electr. Mach. Control*, vol. 19, no. 5, pp. 1–6, 2015.
- [16] S. Nie, F. Lijun, and X. Jin, "Asymmetrical model and parameter calculation of segment-power linear induction motor mover," *J. Nav. Univ. Eng.*, vol. 28, no. 3, pp. 50–54, 2016.
- [17] G. Lv, T. Zhou, and D. Zeng, "Influence of the ladder-slit secondary on reducing the edge effect and transverse forces in the linear induction motor," *IEEE Trans. Ind. Electron.*, vol. 65, no. 9, pp. 7516–7525, Sep. 2018.
- [18] G. Lv, T. Zhou, and D. Zeng, "Influence of the V-type secondary on the air-gap magnetic field and performance of the linear induction motor," *IET Electr. Power Appl.*, vol. 13, no. 2, pp. 229–234, 2018.
- [19] G. Lv, T. Zhou, D. Zeng, and Z. Liu, "Influence of parameters of cap-lamination secondaries on performances in single-sided linear induction motors," *IET Electr. Power Appl.*, vol. 11, no. 3, pp. 393–398, Mar. 2017.
- [20] Q. Lu, Y. Li, Y. Ye, and Z. Q. Zhu, "Investigation of forces in linear induction motor under different slip frequency for low-speed maglev application," *IEEE Trans. Energy Convers.*, vol. 28, no. 1, pp. 145–153, Mar. 2013.
- [21] W. Xu, J. G. Zhu, Y. Zhang, Z. Li, Y. Li, Y. Wang, Y. Guo, and Y. Li, "Equivalent circuits for single-sided linear induction motors," *IEEE Trans. Ind. Appl.*, vol. 46, no. 6, pp. 2410–2423, Nov. 2010.
- [22] W. Xu, J. Guo Zhu, Y. Zhang, Y. Li, Y. Wang, and Y. Guo, "An improved equivalent circuit model of a single-sided linear induction motor," *IEEE Trans. Veh. Technol.*, vol. 59, no. 5, pp. 2277–2289, 2010.
- [23] W. Xu, X. Xiao, G. Du, D. Hu, and J. Zou, "Comprehensive efficiency optimization of linear induction motors for urban transit," *IEEE Trans. Veh. Technol.*, vol. 69, no. 1, pp. 131–139, Jan. 2020.
- [24] E. Amiri and E. A. Mendrela, "A novel equivalent circuit model of linear induction motors considering static and dynamic end effects," *IEEE Trans. Magn.*, vol. 50, no. 3, pp. 120–128, Mar. 2014.



WEICHANG ZHOU received the B.S. and M.S. degrees in electrical engineering from the Naval University of Engineering, Wuhan, China, in 2016 and 2018, respectively, where he is currently pursuing the Ph.D. degree in electrical engineering. His research interest includes design and application for linear motors.



ZHAOLONG SUN received the B.S. and Ph.D. degrees in electrical engineering from the Naval University of Engineering, Wuhan, China, in 2006 and 2011, respectively. In 2013, he joined the Naval University of Engineering, where he is currently an Associate Professor and a Ph.D. Supervisor. His current research interest includes electrical devices and machines, especially the design and control for linear motors.



FENGRUI CUI received the B.S. degree in navigation engineering from the Naval University of Engineering, Wuhan, China, in 2018, where he is currently pursuing the M.S. degree in electrical engineering. His research interest includes design for linear motors.



YINHAO MAO is currently pursuing the M.S. degree in electrical engineering with the Naval University of Engineering, Wuhan, China. His research interest includes design for linear motors.